Supporting Information

Fabrication and Processing of Bacterial Cellulose/Silver Nanowire Composites as Transparent, Conductive, and Flexible Films for Optoelectronic Applications

Denisha Gounden, Michael N. Pillay, Vashen Moodley, Nolwazi Nombona,

*and Werner E. van Zyl**

E-mail: vanzylw@ukzn.ac.za

CONTENTS:

NOTE: The Figures and Tables are labeled and listed chronologically in both the Main text and Supplementary Information. Figures are listed first, followed by Tables. Not all Figures and Tables are discussed in the Main text and are thus provided in the Supplementary section. For convenience, the relevant Figures and Tables per section are indicated below.

Figure S1. (a) Hydrolyzed BC in dialysis socks, (b) dialyzed BC (at pH 6) in dialysis socks and (c) dialyzed BC transferred to glass storage jars.

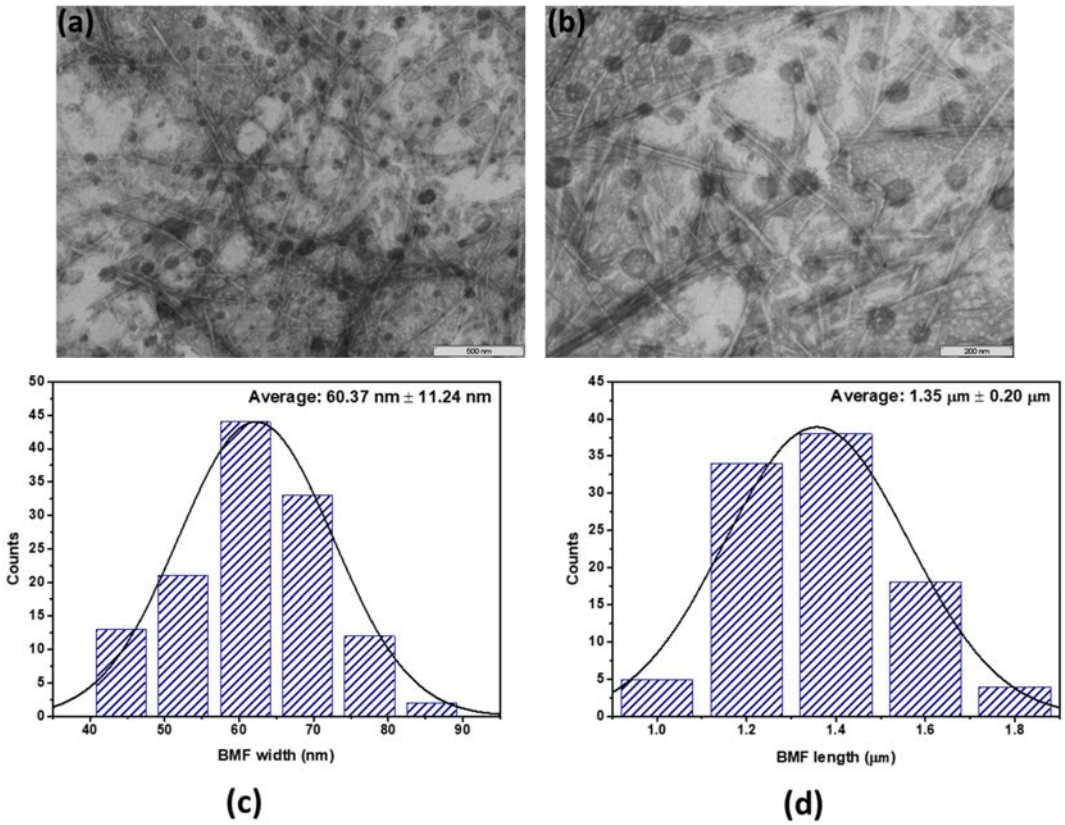

Figure S2. TEM images (a and b), and **s**ize distribution graphs of the BMF widths (c) and BMF lengths (d).

In the low strain portion of the curves, all the films obey Hooke's law to a reasonable approximation, such that stress is proportional to strain. Therefore, it is represented as a linear region in the curve (See insets in Figures S3-S7). The slope of this linear region is quantified as *E*, as seen in Equation S1:

$$E = \frac{\sigma}{\varepsilon} \qquad \text{(Equation S1)}$$

where E is Young's Modulus (MPa), σ is the uniaxial stress (MPa), and ε is strain (dimensionless).

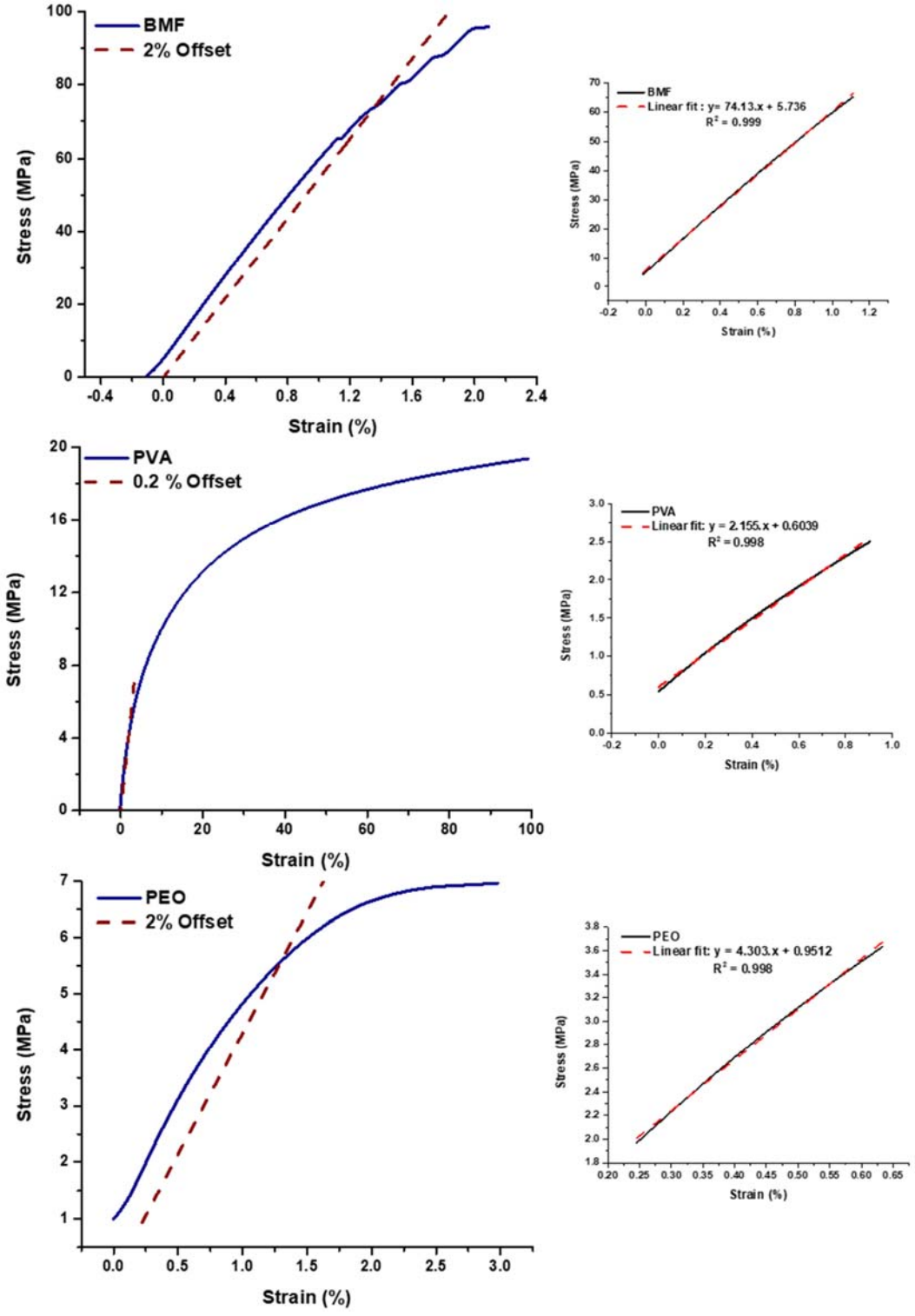

Figure S3. Stress-strain curves for pure BMF, PVA and PEO.

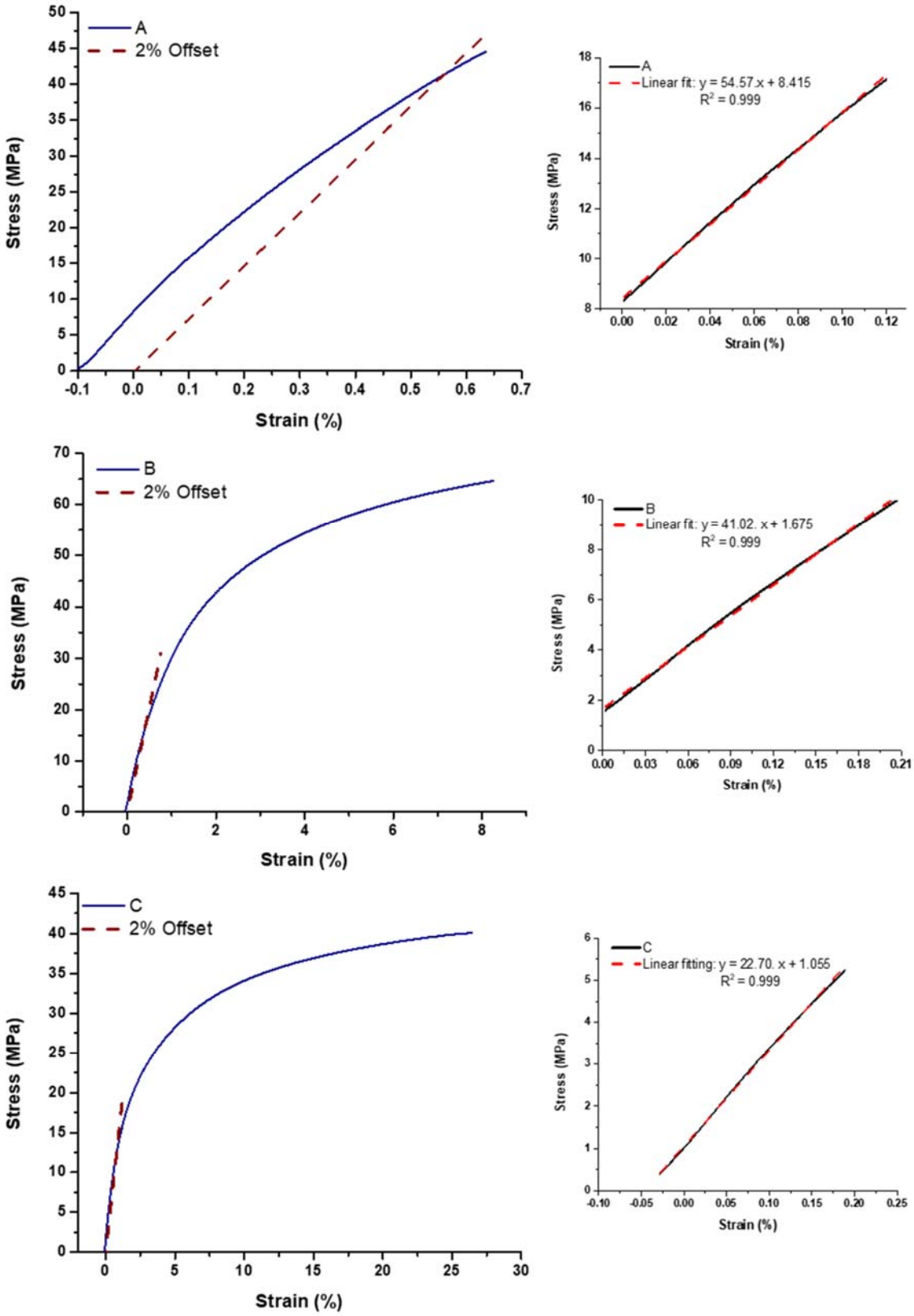

Figure S4. Stress-strain curves and linear fitting (insets) of composites A, B and C.

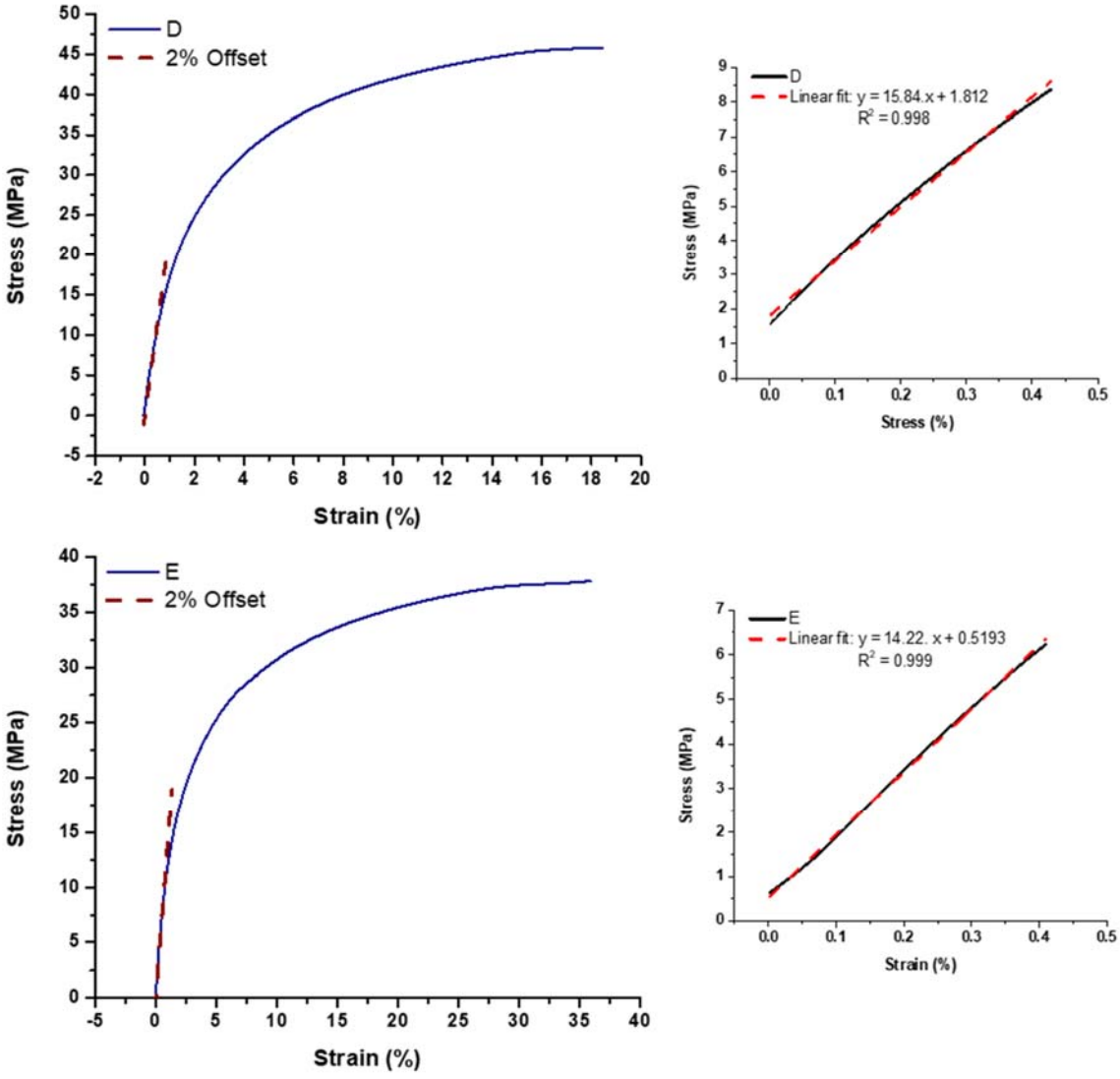

Figure S5. Stress-strain curves and linear fitting (insets) of composites D and E.

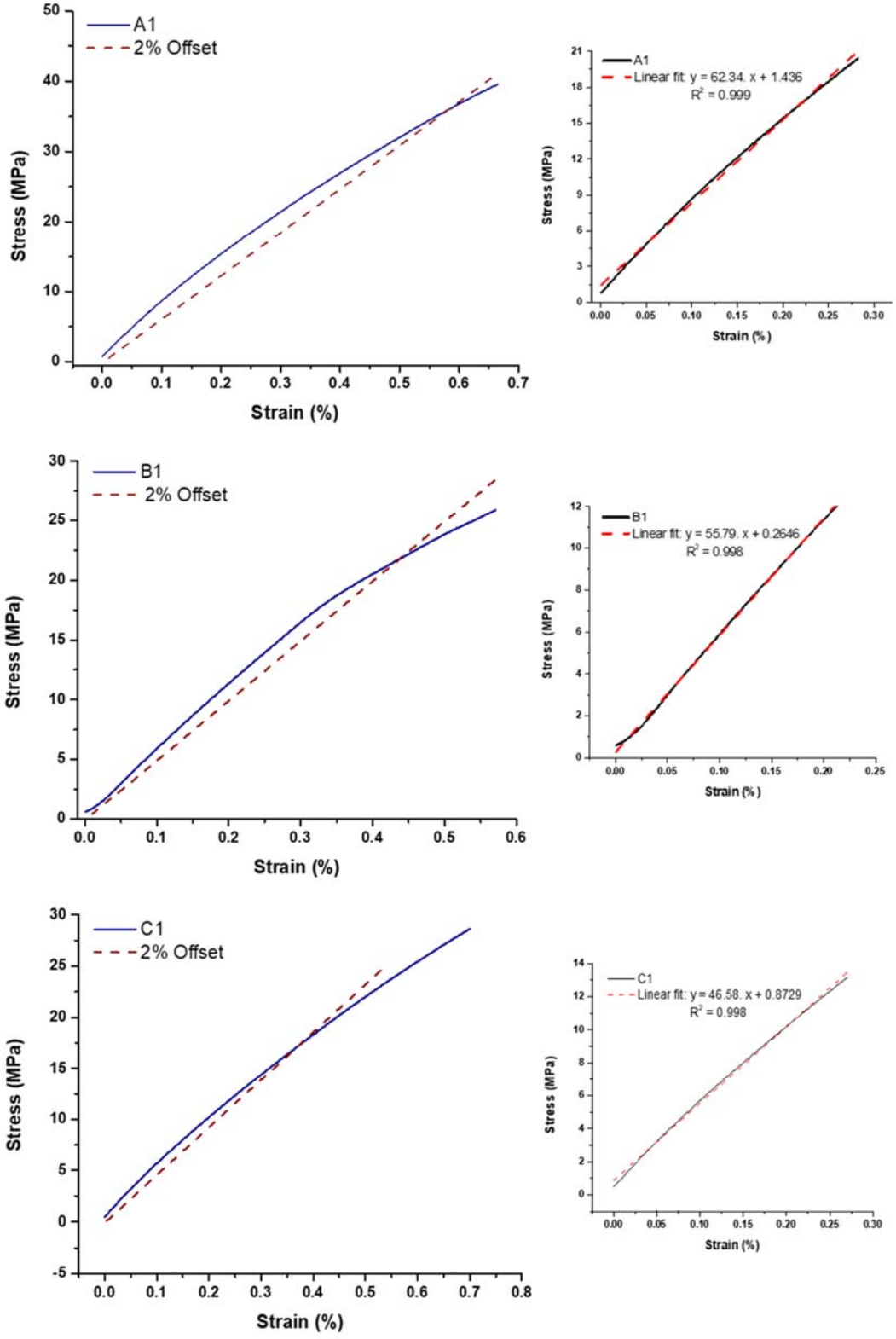

Figure S6. Stress-strain curves and linear fitting (insets) of composites A1, B1 and C1.

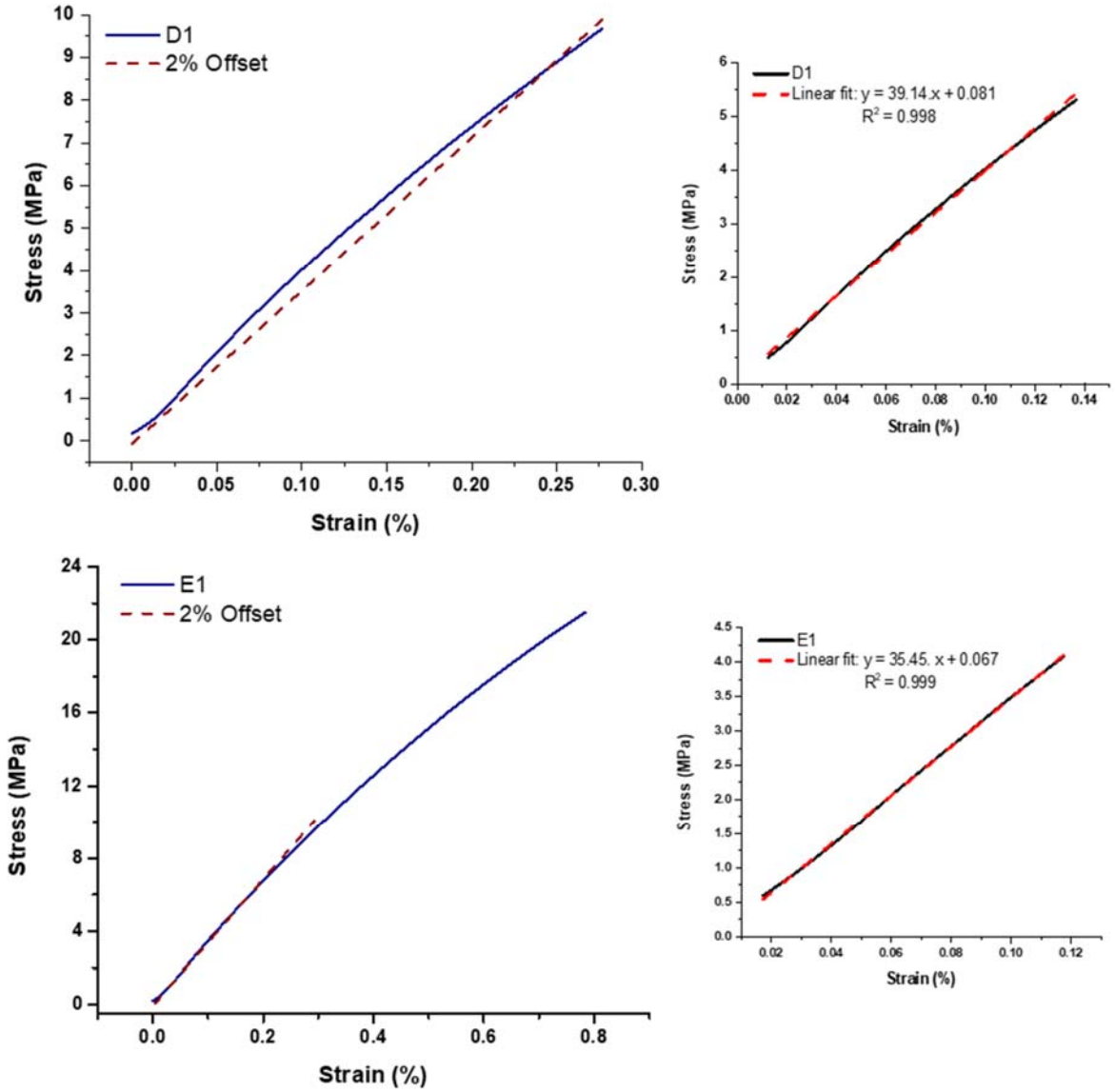

Figure S7. Stress-strain curves and linear fitting (insets) of composites D1 and E1.

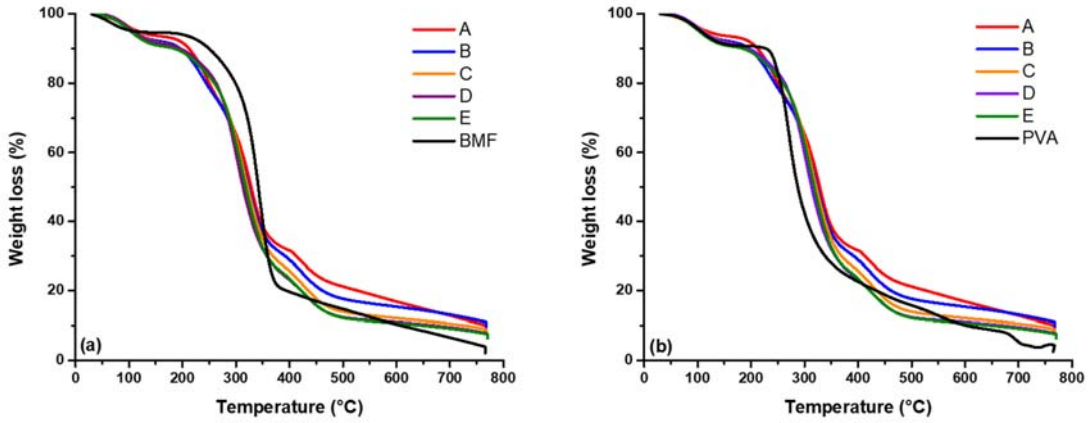

Figure S8. Thermograms for (a) pure BMF with A-E composite films and (b) pure PVA with A-E composite films.

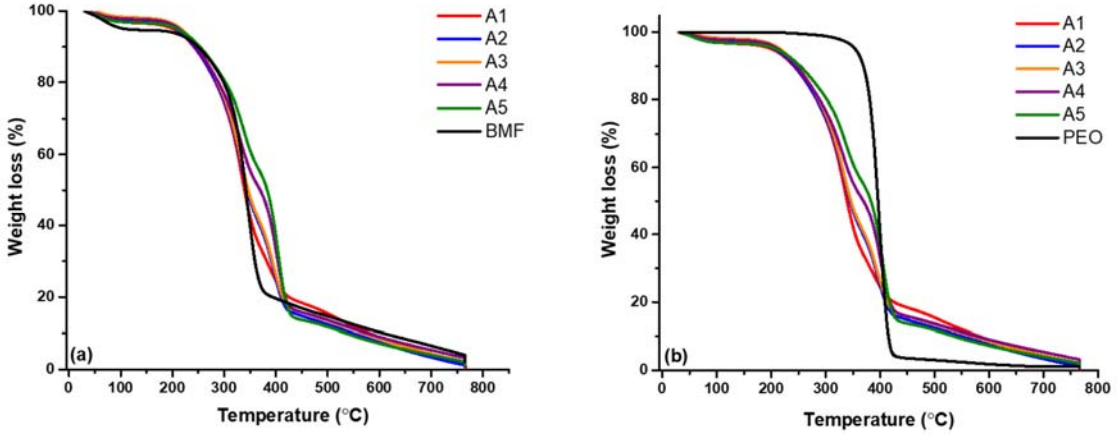

Figure S9. Thermograms for (a) pure BMF with A1-E1 composite films and (b) pure PEO with A1-E1 composite films.

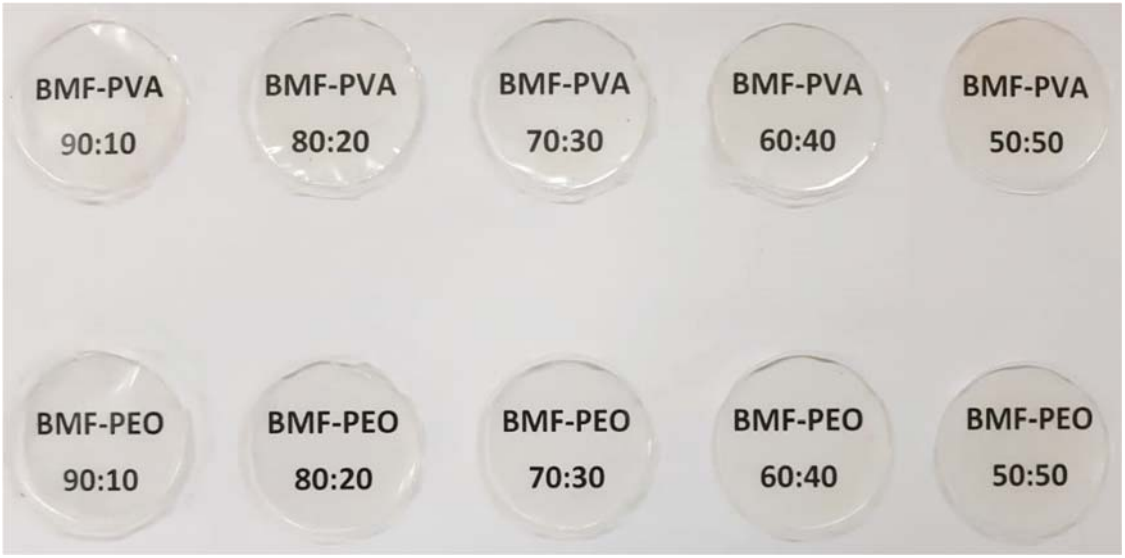

Figure S10. Images depicting the visual transparency of films A-E and A1-E1.

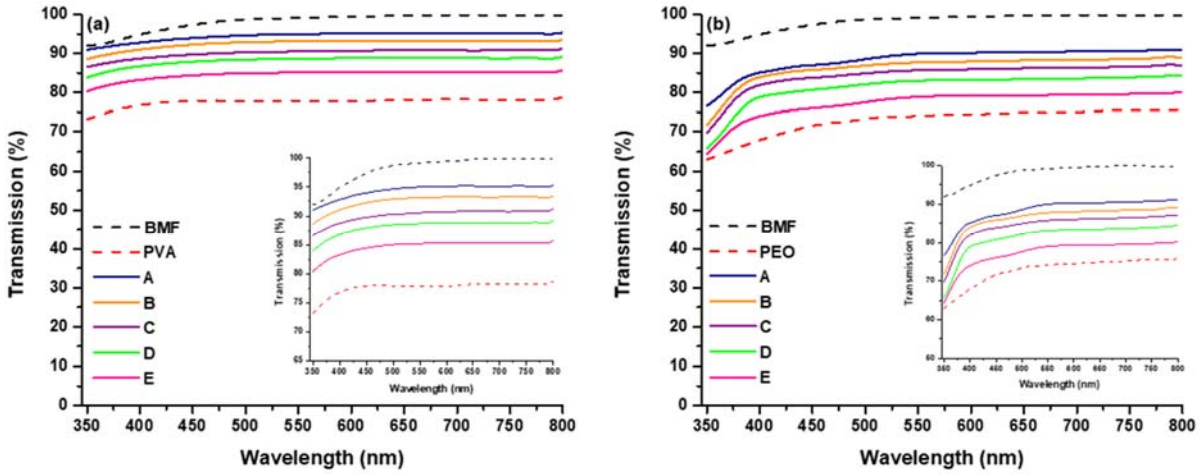

Figure S11. Transmission spectra of films (a) A-E and (b) A1-E1 compared to pure BMF, PVA and PEO.

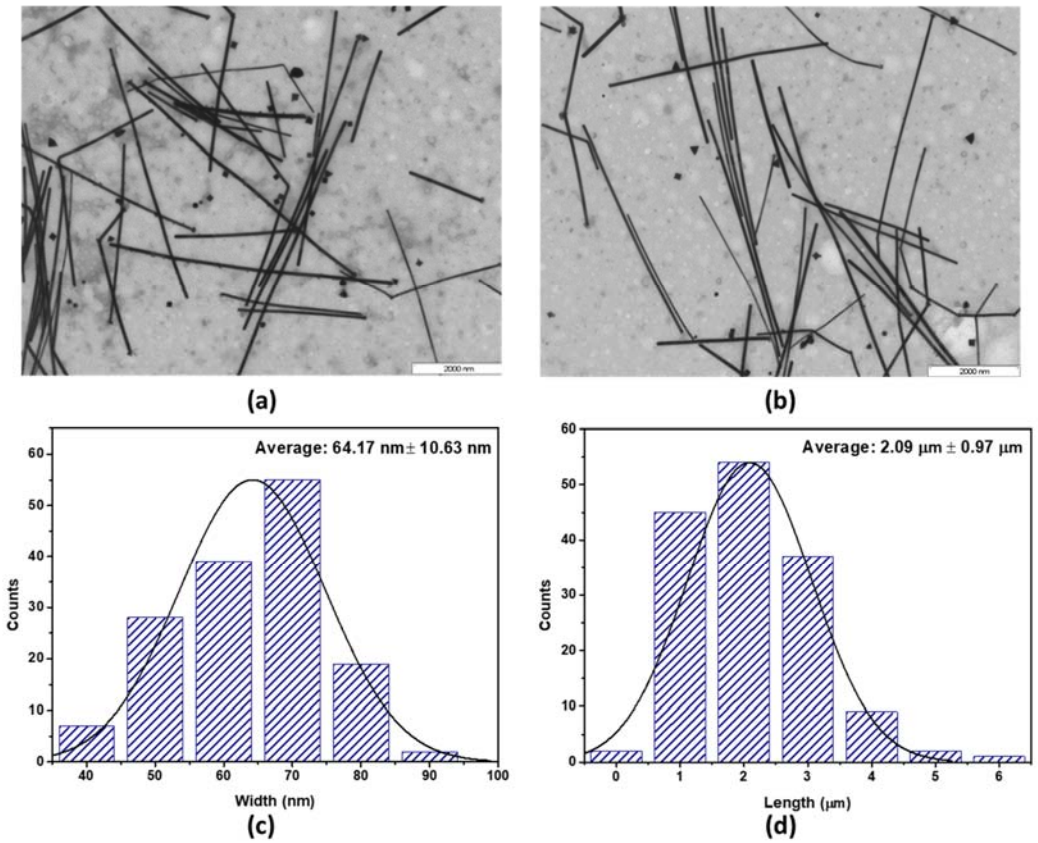

Figure S12. TEM micrographs of AgNWs with a scale bar of 2000 nm (a and b) and size analysis distribution graphs of the (c) AgNW widths and (d) AgNW lengths.

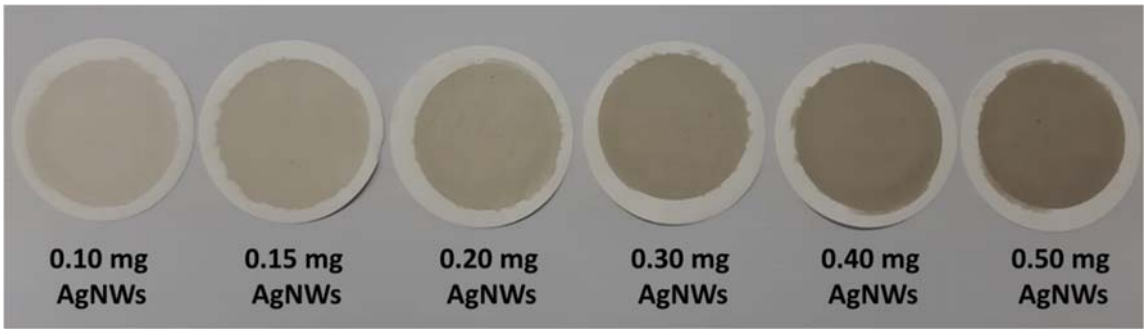

Figure S13. MCE membrane filters with AgNWs.

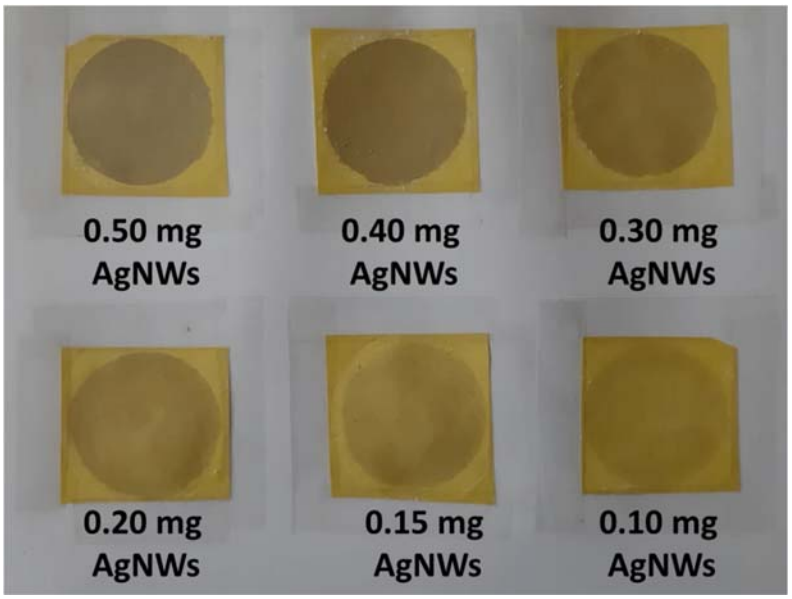

Figure S14. Transfer paper with AgNWs.

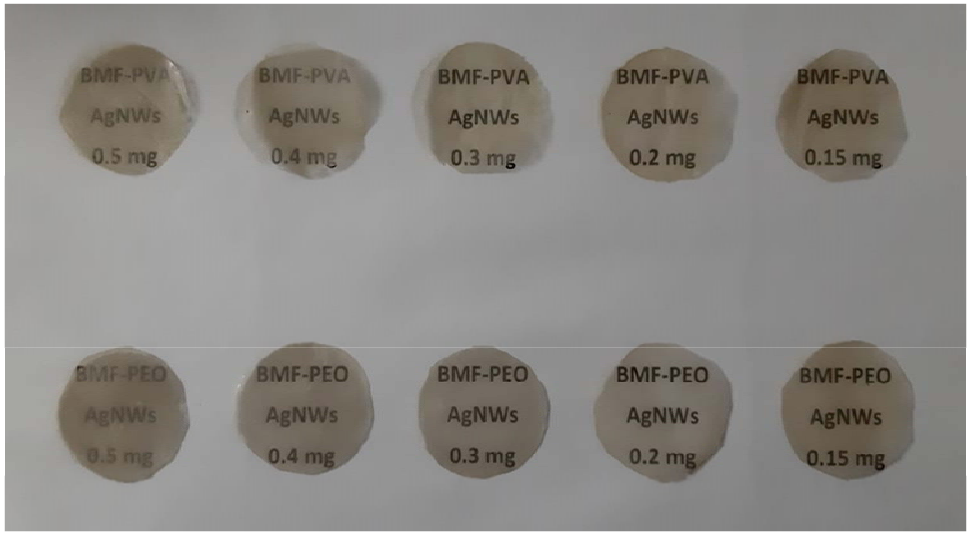

Figure S15. BMF-polymer composite film, (C and C1) coated with varying AgNW loadings.

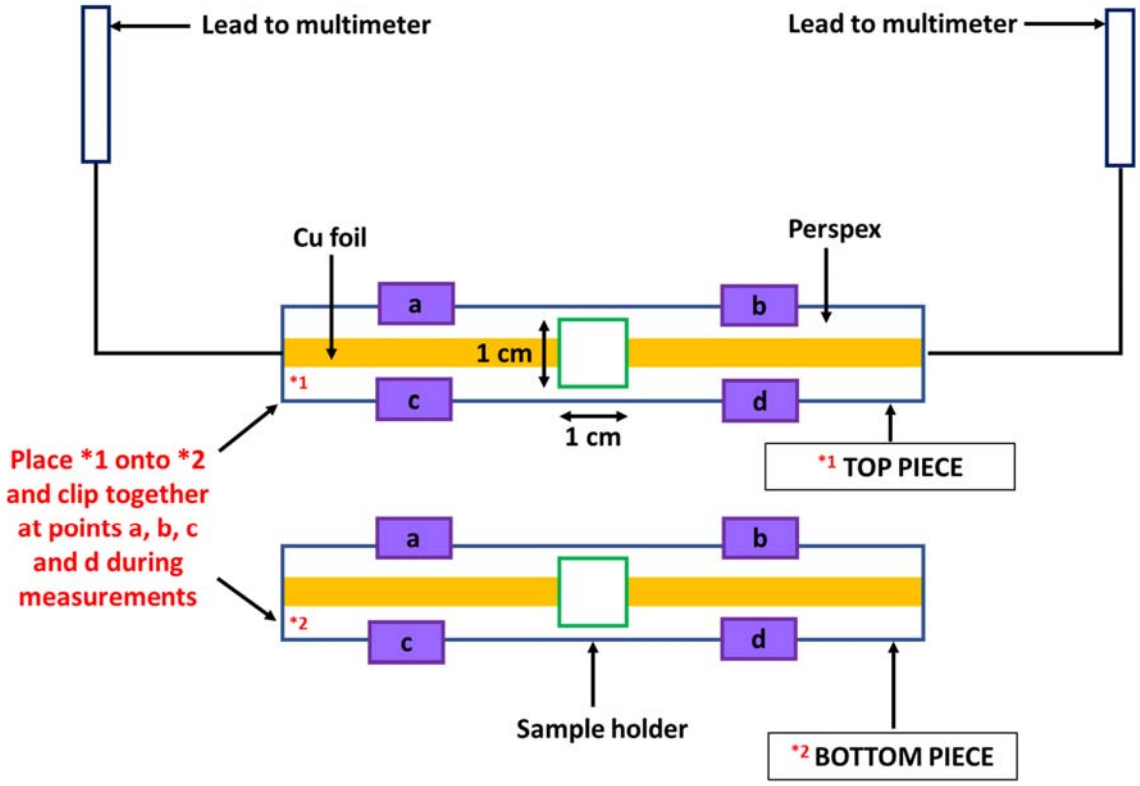

Figure S16. In-house designed resistance apparatus**.**

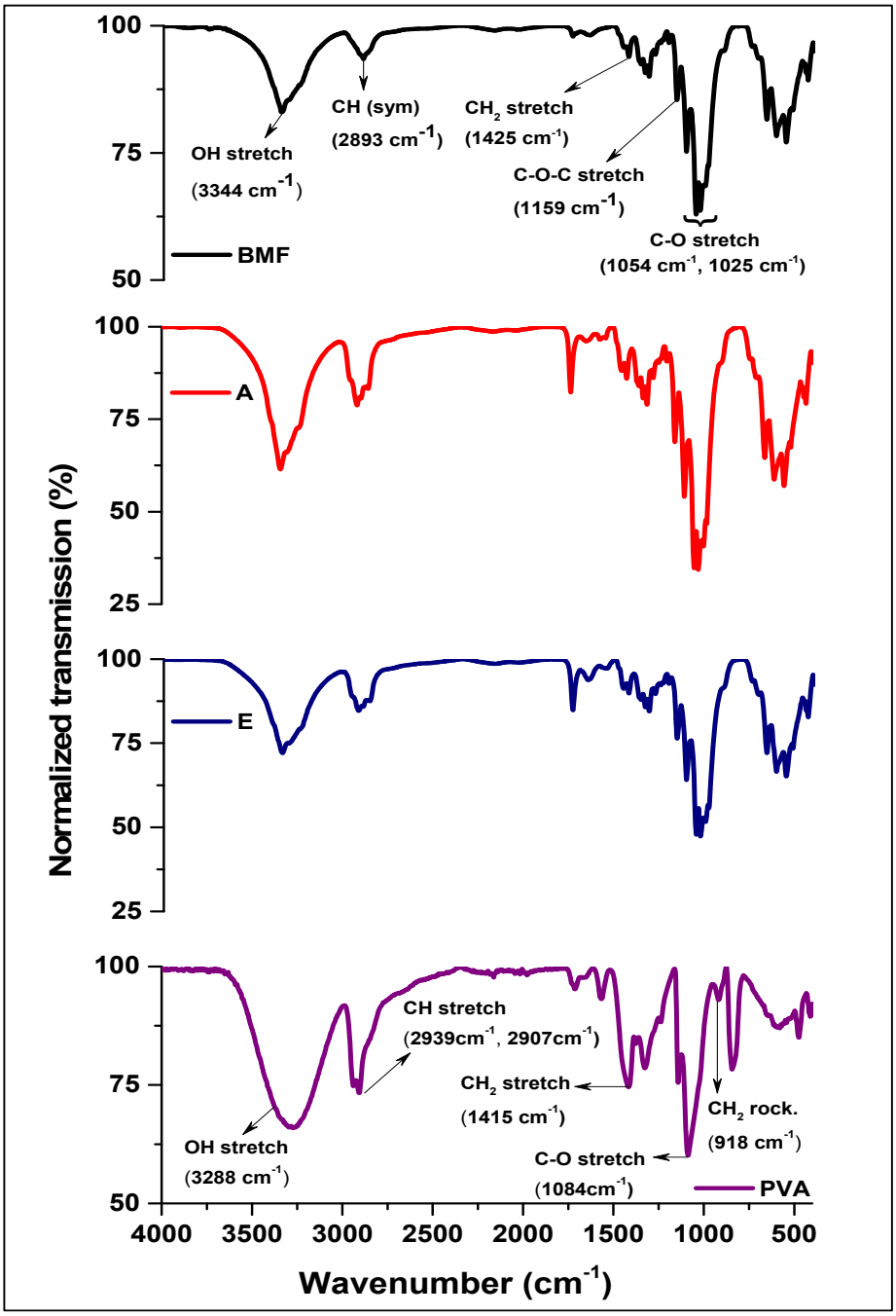

Figure S17. FT-IR spectra of the pure BMF, pure PVA and composite films A and E.

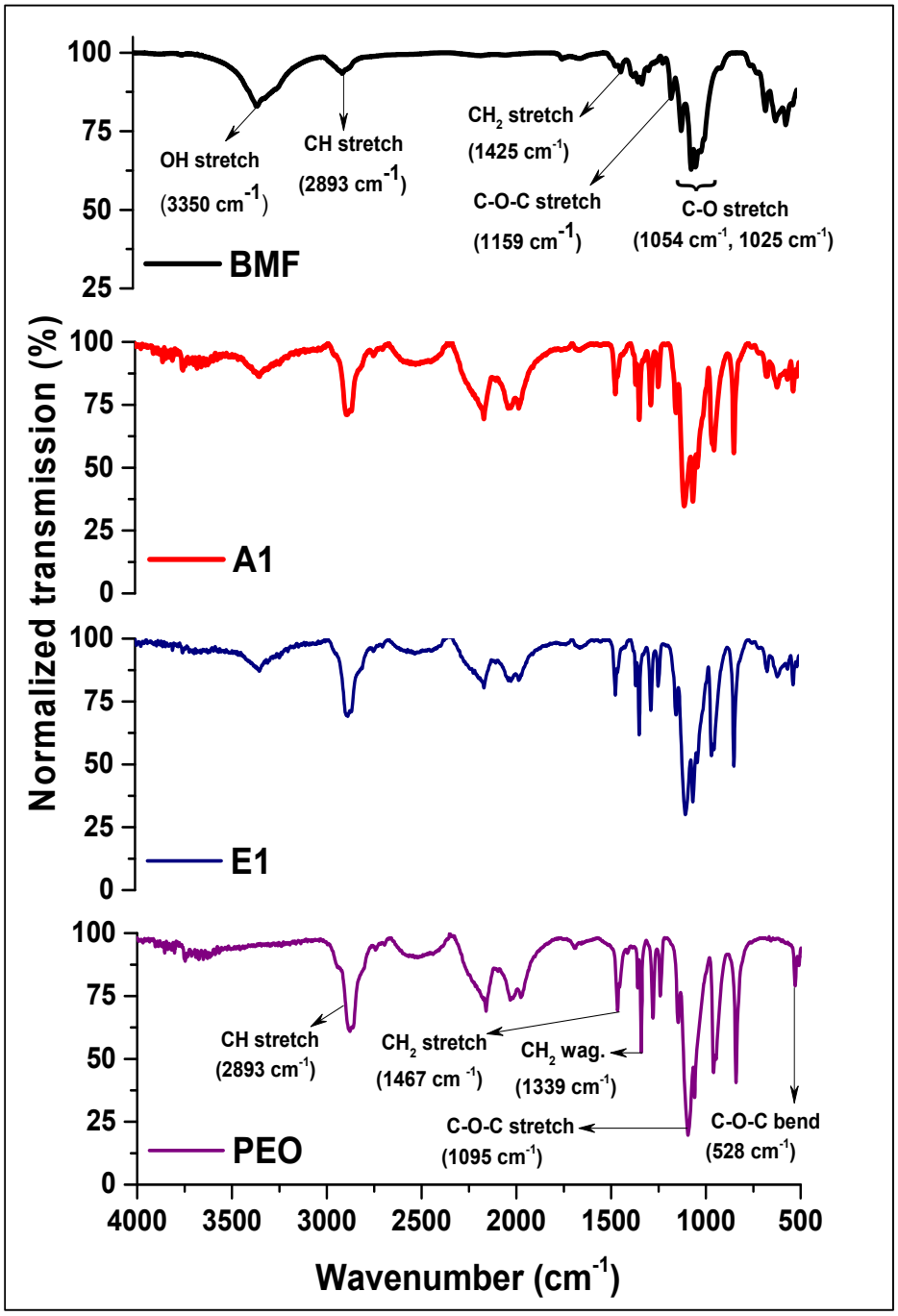

Figure S18. FT-IR spectra of the pure BMF, pure PEO, and composite films A1 and E1.

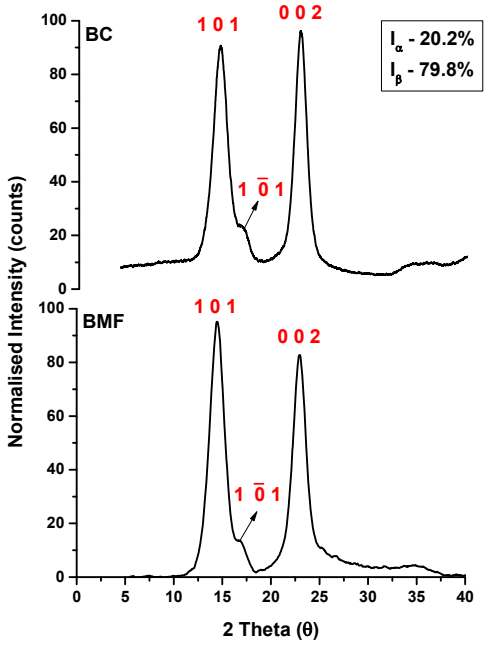

Figure S19. XRD diffractogram of BC and BMF.

AgNW UV-vis Charcerisation:

UV-vis spectroscopy is a simple and sensitive technique used to characterize the formation of synthesized Ag nanoparticles.[1] A unique phenomenon called surface plasmon resonance (SPR) occurs when Ag is exposed to incident light. Surface plasmon resonance arises when free conduction electrons on the silver metal surface collectively oscillate when excited by light at specific wavelengths.[2] The collective oscillations of the free electrons can either cause strong scattering or resonate with the light wave, resulting in the absorption of light at a particular wavelength.[1,3] The absorption profile of Ag nanoparticles depends upon the size and morphology of the synthesized nanoparticle, i.e., sphere, rod, cube, wire, film, etc.[2] Figure S20 displays the UV-vis spectra of AgNWs in EtOH at different concentrations. An absorption peak at 453 nm and a characteristic shoulder at 355 nm confirmed the formation of the AgNWs.[4,5] These peaks were observed for all concentrations and showed increased absorption with increasing AgNW concentration.

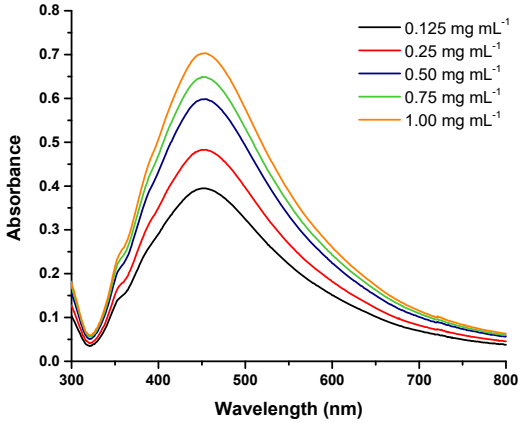

Figure S20. UV-vis spectra of AgNWs in EtOH at varying concentrations.

$$(ahv)^n = K\,(hv - E_g) \qquad \text{(Equation S2)}$$

where α is the absorption coefficient, h is Planck's constant, ν is the photon's frequency, K is an energy-dependent constant, E_g is the bandgap, and the exponent n represents the nature of the transition and may take on values $n = \frac{1}{2}, 1, \frac{3}{2}$ or 2, depending upon the nature of the electronic transitions (i.e., allowed or forbidden) responsible for the absorption. The direct optical energy bandgap (Eg) was estimated by extrapolating the linear portion of the curve $(\alpha h\nu)^2$ against (hν) for direct allowed transition to the point where αhν = 0 as shown in Figure S21. Using n = 2, the E_g of the AgNWs was observed at 2.01 eV.

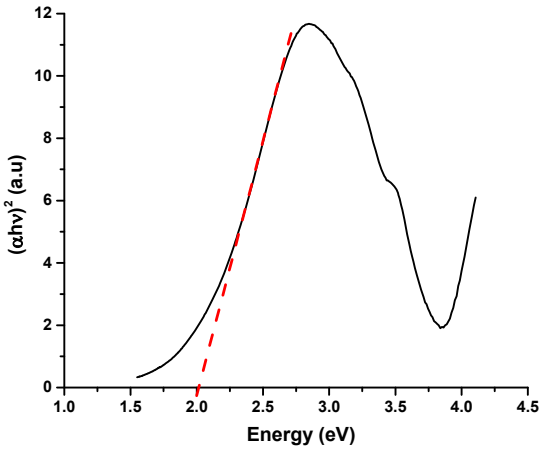

Figure S21. Tauc plot of AgNWs (1.0 mg mL^{-1}).

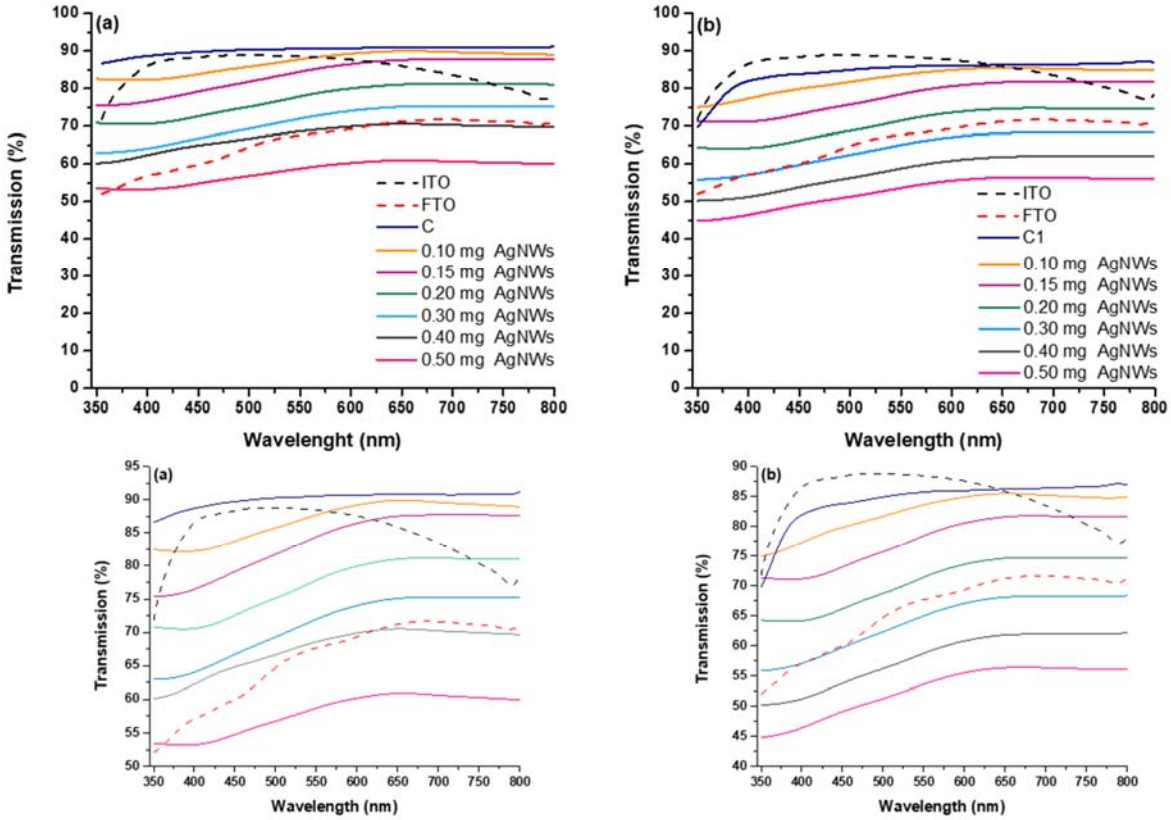

Figure S22. Optical transmission of BMF-polymer-AgNWs films with different Ag loadings.

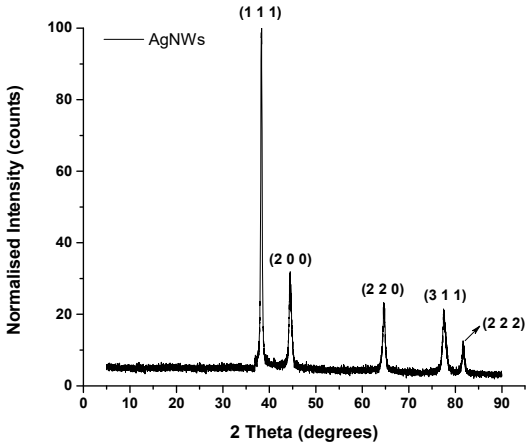

Figure S23. XRD diffractogram of AgNWs.

The FCC theoretical lattice constant (a) was calculated for the AgNWs using the following formula [6]:

$$Theoretical\ lattice\ constant, a = \frac{4\ x\ r}{(2)^{1/2}} = \frac{4\ x\ 0.144}{2^{1/2}} = 0.4073 \qquad \text{(Equation S3)}$$

where r is the atomic radius of the atoms in the unit cell. The atomic radius of Ag is 0.144 nm. The experimental a is calculated using the d-spacing parameter from the most intense peak (111) of the diffractogram using this formula reserved for cubic structures:

$$\frac{1}{d^2} = \frac{h^2+k^2+l^2}{a^2} \qquad \text{(Equation S4)}$$

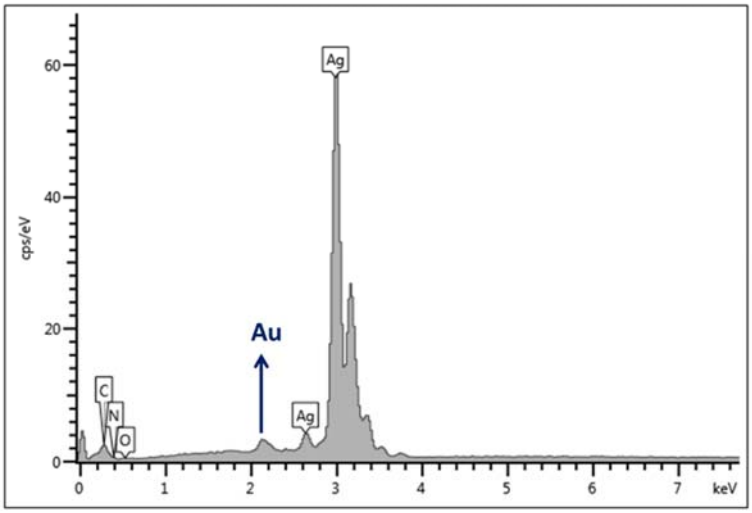

Figure S24. EDX spectrum of AgNWs.

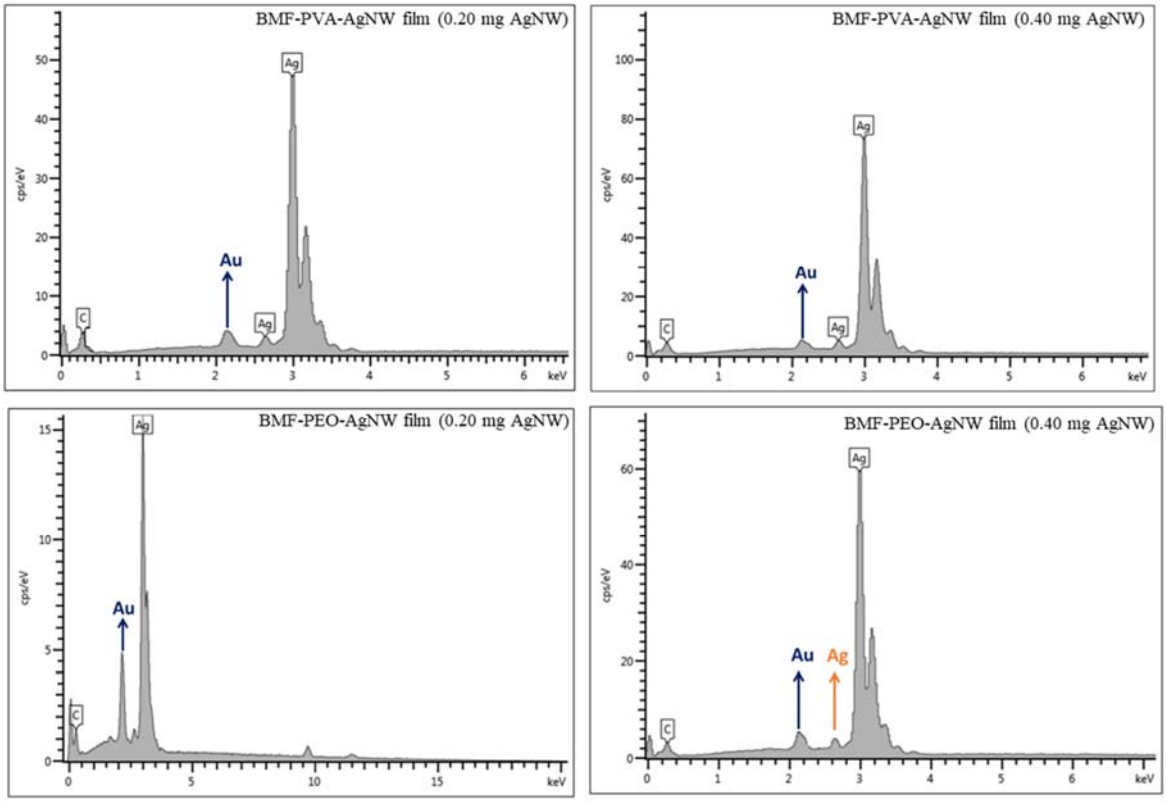

Figure S25. EDX spectra of the BMF-PVA-AgNW films and BMF-PEO-AgNW films.

Table S1. Diffraction peaks for pure BMF, pure PVA, composite films A-E and crystallinity index of cellulose in BMF and composite films A-E.

Films	2 θ (°)					CrI (%) (for cellulose)
	PVA peaks		Cellulose peaks			
	(1 0 $\bar{1}$) and (1 0 1)	(2 0 0)	(1 0 1)	(1 $\bar{0}$ 1)	(2 0 0)	
BMF	-	-	14.45	16.78	22.94	99.00
PVA	19.48	20.84	-	-	-	-
A	19.89	-	15.22	16.55	23.01	83.75
B	19.80	-	15.08	16.60	22.83	81.49
C	19.72	-	15.00	16.76	22.74	78.12
D	19.80	-	15.36	16.76	22.86	76.48
E	20.13	-	15.25	17.10	23.08	72.30

Table S2. Diffraction peaks for pure BMF, pure PEO and composite films A1-E1.

Films	2 θ (°)				
	PEO peaks		Cellulose peaks		
	(1 2 0)	(1 1 1)	(1 0 1)	(1 $\bar{0}$ 1)	(2 0 0)
BMF	-	-	14.45	16.78	22.94
PEO	19.35	23.59	-	-	-
A1	-	-	15.06	16.59	22.88*
B1	-	-	15.19	16.84	23.07*
C1	-	-	15.04	16.37	23.11*
D1	-	-	15.09	16.66	23.14*
E1	19.66	-	15.18	16.66	23.16*

*peaks could not be deconvoluted for accurate plane assignment between the (1 1 1) plane of PEO and the (2 0 0) plane of BMF.

The crystallinity index (*CrI%*) evaluates the amount of crystalline and amorphous content within the cellulose samples.[7] The method used was developed by Segal *et al*. and calculates the percentage crystallinity by using the ratio of the height of the most intense peak (I_{max}, which represents the crystalline part of the BMF film) and the minimum height between the I_{max} and the adjacent peak (I_{am}, represents the amorphous part of the BMF film).[8] From Table S1, although the samples show high crystallinity percentages, a decrease in crystallinity is observed with an increase in the PVA weight percentage, which is expected. The *CrI%* of cellulose in films A1-E1 could not be calculated due to the ambiguous nature of the (2 0 0) peak.

Table S3 further displays calculated d-spacing *(d)* and crystallite size *(L)* parameters of the BC and BMF films. These parameters could not be accurately determined for the other films due to

their composite nature. Although there has been precedent for calculating the average crystallite size using the Scherrer equation, there are issues concerning the curve fitting ranges and the size and placement of the amorphous halo of the cellulose.[9] The d-spacing between the BC and BMF displays little variation and indicates that the planes of the BMF remain relatively unchanged after alkaline and acid hydrolysis treatment. The Scherrer equation (Equation S5) was used to determine crystallite sizes:

Using the (0 0 2) diffraction peak for BC and BMF, the crystalline sizes were evaluated using Scherrer's equation:

$$\beta = \frac{K.\lambda}{\tau\,.\,cos\theta} \qquad \text{(Equation S5)}$$

Where β is the full width at half maximum (FWHM) of the XRD peaks, k = 0.94 (dimensionless shape factor), λ is the wavelength of the incident X-rays, τ is the crystallite size, and θ is the diffraction angle corresponding to the planes.

The BC presented with a crystallite size of 6.09 nm. In comparison, BMF had a decreased crystallite size of 4.54 nm, suggesting that the concentration of H_2SO_4 (60 wt.%) and/or the hydrolysis duration affects the crystallite size of the resultant BMF.[10] The molecular chains of the BC may be rearranged during acid hydrolysis, and these rearrangements could result in smaller crystallite sizes.[11]

Table S3. d-spacing and crystallite size computed from the XRD patterns for BC and BMF films.

Films	Peaks (*2θ*)°	*d* (nm)	*L* (nm)
BC	14.67	0.6081	6.09
	16.79	0.5319	
	22.76	0.3894	
BMF	14.45	0.6124	4.54
	16.86	0.5255	
	22.94	0.3872	

Table S4. Young modulus (*E*) and yield strength (σY) derived from stress-strain curves of all films

	Young modulus (MPa)	Yield strength (MPa)	Film	Young modulus (MPa)	Yield strength (MPa)
BMF	74.13	73.96			
A	54.56	41.36	A1	62.34	36.12
B	41.02	16.32	B1	57.38	21.79
C	22.70	12.39	C1	46.58	17.66
D	15.84	9.544	D1	39.14	8.643
E	14.22	8.715	E1	35.45	7.497
PVA	2.155	4.122	PEO	4.303	5.583

Table S5. Major decomposition temperatures extracted from TGA thermograms.

Films	Major decomposition temperature (°C)
BMF	220
PVA	227
A	190
B	188
C	188
D	188
E	187
PEO	339
A1	216
B1	213
C1	213
D1	213
D1	213

Table S6. Diffraction peaks for AgNWs, BMF-polymer films (C and C1) and, BMF-polymer-AgNWs films (C + 0.20 AgNWs, C + 0.40 AgNWs, C1 + 0.20 AgNWs and C1 + 0.40 AgNWs).

Sample	2 θ (°)								
	PVA peaks		PEO peaks		Cellulose peaks			Ag peaks	
	(1 0 $\bar{1}$) (1 0 1)	(2 0 0)	(1 2 0)	(1 1 1)	(1 0 1)	(1 $\bar{0}$ 1)	(2 0 0)	(1 1 1)	(2 0 0)
AgNWs								38.29	44.50
C	19.72	-			15.00	16.76	22.74		
C1			-	-	15.04	16.37	23.11*		
C + 0.20 mg Ag	19.71	-			15.03	16.73	22.73	38.20	44.45
C + 0.40 mg Ag	20.03	-			15.13	17.10	23.08	38.22	44.43
C1 + 0.20 mg Ag			-	-	15.00	16.31	23.07*	38.18	44.47
C1 + 0.40 mg Ag			-	-	15.03	16.39	23.07*	38.27	44.47

*peaks could not be deconvoluted for accurate plane assignment between the (1 1 1) plane of PEO and the (2 0 0) plane of BMF.

Table S7. Ratios of BMF to polymer in the composite films.

Polymer	Ratio of BMF: Polymer		BMF (10 mg mL^{-1})		Polymer (5 wt%)		Total weight of film	
							Expected	Actual
			mL	mg	µL	mg	mg	mg
	Reference	100: 0	5.0	50	0	0	50	49.84 ± 0.06
PVA	A	90: 10	4.5	45	100	5	50	49.89 ± 0.01
	B	80: 20	4.0	40	200	10	50	49.95 ± 0.05
	C	70: 30	3.5	35	300	15	50	49.97 ± 0.06
	D	60:30	3.0	30	400	20	50	50.02 ± 0.05
	E	50:50	2.5	25	500	25	50	50.06 ± 0.06
PEO	A1	90: 10	5.0	50	100	5	50	49.83 ± 0.06
	B1	80: 20	4.5	45	200	10	50	49.93 ± 0.06
	C1	70: 30	4.0	40	300	15	50	50.03 ± 0.06
	D1	60:30	3.5	35	400	20	50	49.87 ± 0.05
	E1	50:50	3.0	30	500	25	50	50.07 ± 0.06

Table S8. Varying amounts of AgNW used to coat the optimised BMF-polymer films (C and C1).

Amount of AgNWs to be transferred to film (mg)	Volume of AgNW stock soln. required (μL)	Volume of ddH_2O added (mL)	Final volume (mL)
0	0	25.00	25.0
0.10	100	24.90	25.0
0.15	150	24.85	25.0
0.20	200	24.80	25.0
0.30	300	24.70	25.0
0.40	400	24.60	25.0
0.50	500	24.50	25.0

Table S9. Elemental composition of the BMF-polymer-AgNWs films.

Films	Elemental composition (%)		
	C	O	Ag
C + 0.20 mg AgNWs	8.22	1.89	89.89
C + 0.40 mg AgNWs	3.94	-	96.04
C1 + 0.20 mg AgNWs	9.51	-	90.49
C1 + 0.40 mg AgNWs	3.98	-	96.02

References

[1] A. O. Dada, F. A. Adekola, O. S. Adeyemi, O. M. Bello, A. C. Oluwaseun, O. J. Awakan, F.-A. A. Grace, Ed. F. A. Adekola, IntechOpen, Rijeka, **2018**, p. Ch. 9, DOI: 10.5772/intechopen.76947.

[2] V. Amendola, O. M. Bakr, F. Stellacci, *Plasmonics* **2010**, *5*, 85, DOI: 10.1007/s11468-009-9120-4.

[3] D. A. Skoog, F. J. Holler, S. R. Crouch, 'Principles of instrumental analysis', Belmont Brooks/Cole, CA: Thomson, **2007**.

[4] M. R. Johan, N. A. K. Aznan, S. T. Yee, I. H. Ho, S. W. Ooi, N. Darman Singho, F. Aplop, *J. Nanomater.* **2014**, *2014*, 105454, DOI: 10.1155/2014/105454.

[5] B. Liu, H. Yan, S. Chen, Y. Guan, G. Wu, R. Jin, L. Li, *Nanoscale Res. Lett.* **2017**, *12*, 212, DOI: 10.1186/s11671-017-1963-6.

[6] T. Theivasanthi, M. Alagar, *Nano Biomed. Eng.* **2012**, *4*, 58, DOI: 10.5101/nbe.v4i2.p58-65.

[7] S. Park, J. O. Baker, M. E. Himmel, P. A. Parilla, D. K. Johnson, *Biotechnol. Biofuels* **2010**, *3*, 10, DOI: 10.1186/1754-6834-3-10.

[8] L. Segal, J. J. Creely, A. E. Martin, C. M. Conrad, *Text. Res. J.* **1959**, *29*, 786, DOI: 10.1177/004051755902901003.

[9] Q. Li, S. McGinnis, C. Sydnor, A. Wong, S. Renneckar, *ACS Sustain. Chem. Eng.* **2013**, *1*, 919, DOI: 10.1021/sc4000225.

[10] K. Kafle, H. Shin, C. M. Lee, S. Park, S. H. Kim, *Sci. Rep.* **2015**, *5*, 15102, DOI: 10.1038/srep15102.

[11] J. Gong, J. Li, J. Xu, Z. Xiang, L. Mo, *RSC Adv.* **2017**, *7*, 33486, DOI: 10.1039/C7RA06222B.